AGU ADVANCING EARTH AND SPACE SCIENCES

Deciphering Permanent Uplift Along the Pacific Coast of South America Through Signal Analysis of Various Tectonic Processes

Roland Freisleben[1] , Julius Jara-Muñoz[2] , Daniel Melnick[3,4] , Diego Molina[4,5], Andrés Tassara[4,5] , Peter van der Beek[1] , and Manfred R. Strecker[1]

[1]Institut für Geowissenschaften, Universität Potsdam, Potsdam, Germany, [2]Faculty of Civil Engineering, Hochschule Biberach, Biberach an der Riß, Germany, [3]Instituto de Ciencias de la Tierra, TAQUACH, Universidad Austral de Chile, Valdivia, Chile, [4]Millennium Nucleus CYCLO, Valdivia, Chile, [5]Departamento Ciencias de la Tierra, Facultad de Ciencias Químicas, Universidad de Concepción, Concepcion, Chile

Abstract The tectonically active South American margin is characterized by the accumulation of deformation contributing to uplift of the Andean forearc at millennial time scales. However, the mechanisms responsible for permanent coastal uplift are debated, mainly because methodologically consistent, continental-scale analyses of uplifted terraces have not yet been carried out for South America. Uplifted marine terraces are generally used to infer permanent coastal deformation and uplift; we used almost 2,000 measurements of last-interglacial marine terraces to calculate an uplift-rate signal on which we performed a wavelength analysis. The same spectral analysis was applied to tectonic and subduction parameters associated with accumulation of permanent deformation to detect possible links with the uplift-rate signal. The uplift-rate signal displays a constant background-uplift rate along the margin, perturbed by changes at variable wavelengths. Similarities between its wavelength spectrum and the spectra of tectonic parameters suggest potential correlations pointing toward underlying processes. For example, crustal faulting is mainly responsible for short-wavelength deformation; intermediate-wavelength to long-wavelength tectonic features indicate various extents of locked areas on the megathrust that relate to its long-term seismotectonic segmentation. We suggest that moderate, long-term background uplift is caused by major, deep earthquakes near the Moho, although records of such events are sparse. Due to their disparate occurrence, we infer accumulation of permanent deformation over millennial time scales through multiple, distinct uplift phases that are spatially and temporally distributed. Our study highlights the application and utility of a signal-analysis approach to elucidate the mechanisms driving surface deformation in subduction zones at a continental scale.

1. Introduction

Multiple marine terraces and strandlines along the tectonically active coast of western South America record the accumulation of deformation that contributes to uplift of the Andean forearc at a variety of time scales (Darwin, 1846; Hsu, 1992; Jara-Muñoz et al., 2015; Melnick, 2016; Pedoja et al., 2014; Regard et al., 2010; Saillard et al., 2011; Wesson et al., 2015). The processes proposed to explain forearc deformation in this geodynamic setting include the subduction of bathymetric anomalies (Hsu, 1992; Martinod et al., 2016; Pedoja et al., 2006; Saillard et al., 2011), upper-plate deformation (Adam & Reuther, 2000; Armijo & Thiele, 1990; Armijo et al., 2015), underplating of subducted trench sediments (Bangs et al., 2020; Clift & Hartley, 2007; Glodny et al., 2005; Melnick & Echtler, 2006; Menant et al., 2020), and the motion of forearc slivers (Jara-Muñoz et al., 2015; Melnick et al., 2009). Importantly, while some authors propose successive earthquakes as a possible cause for coastal uplift (González-Alfaro et al., 2018; Melnick, 2016; Melnick et al., 2006), others suggest that uplift is achieved through interseismic deformation (Allmendinger & González, 2010; Jolivet et al., 2020; Madella & Ehlers, 2021). The different processes addressed here are not mutually restrictive, and in all likelihood a combination of different mechanisms may be responsible for deformation and uplift of coastal areas. However, the relative significance of individual mechanisms for long-term coastal uplift remains debated and analyses of continental-scale deformation patterns along the South American convergent margin are lacking, thus leaving two fundamental questions open: (a) What mechanisms control the accumulation of permanent deformation in the coastal forearc? (b) When does coastal permanent deformation accumulate? These two questions are fundamental to our understanding of tectonically active coastal regions, not only in South America but also on a global scale.

Clarification of these issues is central to the assessment of coastal tectonic landforms and their use in deciphering the characteristics of long-term plate-boundary tectonism, but also to seismogenesis and associated hazards on much shorter time scales that include, e.g., the earthquake cycle.

Along tectonically active coasts, the signal of permanent deformation at 10^4–10^6 year time scales is preserved in the morphology of marine terraces that have evolved through the interplay between wave erosion and coastal retreat, tectonic uplift/subsidence, and climate-controlled, glacial-cycle sea-level oscillations (e.g., Lajoie, 1986). Marine terraces formed during the last interglacial, ~125 kyr ago, are some of the most prominent and widely distributed coastal landforms (Pedoja et al., 2011; Siddall et al., 2006), which have been used extensively to estimate long-term coastal uplift rates (Jara-Muñoz et al., 2015; Muhs et al., 2014; Pedoja et al., 2011; Saillard et al., 2011). However, varying methodological approaches to measure terrace elevation, coupled with discontinuous surveys focused primarily on locations with good terrace preservation, have largely prevented regional comparisons and lateral correlations of uplifted terraces along the western coast of South America. The recently published database of Freisleben et al. (2021), which includes almost 2,000 elevation measurements of the last interglacial terrace level in western South America, affords an opportunity to detect potential correlations between coastal deformation and the underlying tectonic mechanisms on a continental scale.

In this study, we performed spectral analysis to test for possible links between the uplift-rate signal of marine terraces along the western South American coast and various tectonic processes that have been proposed to be responsible for the accumulation of permanent deformation in the Andean forearc. Similar continental-scale parameter comparisons have been conducted at other subduction margins (e.g., Malatesta et al., 2021; Rousset et al., 2016). To analyze spectral similarities between the individual signals, we carried out multiple signal analyses using Fast Fourier Transforms (FFT). Spectral correlations between uplift rate and multiple tectonic parameters revealed potential mechanisms responsible for different wavelengths of permanent deformation. With respect to the mechanisms being responsible for the continuous background signal of uplift rate along the western South American margin, we tested the hypothesis of Melnick (2016) and compared it to predictions of coastal uplift patterns by Jolivet et al. (2020). Melnick (2016) proposed major, deep earthquakes (M7–M8, ~35–55-km depth) down-dip of the interseismically locked megathrust to accumulate anelastic and therefore permanent deformation. This hypothesis thus argues for a disconnect between coastal deformation and the seismic cycle of megathrust earthquakes on the plate interface. In contrast, Jolivet et al. (2020) suggested that a small portion of the geodetically measured interseismic uplift translates into permanent deformation. These two hypotheses thus make contrasting predictions as to when permanent deformation accumulates; we addressed this problem by comparing long-term uplift rates with cumulative vertical displacements of major, deep earthquakes as well as interseismic uplift rates. Our study features a new methodological approach and provides novel perspectives to further elucidate the role of tectonic processes with respect to the evolution of active continental margins at glacial-cycle time scales.

2. Geologic and Tectonic Setting

2.1. Coastal Geomorphology and Marine Terraces Along the Western South American Coast

The ~8,000-km-long Andean orogen constitutes the major physiographic feature of the western South American continent. It is divided by the Huancabamba and Arica Bends into distinctive geomorphic segments with different tectonic characteristics (Figure 1a; Jaillard et al., 2000). From north to south along the western South American coast, the relatively wide (50–180 km) coastal area of the NNE-SSW-trending Ecuadorian Andes is characterized by relatively low relief (<300 m a.s.l.) and separated from the southern forearc by the Dolores-Guayaquil Megashear (DGM). The NW-SE-oriented Peruvian segment comprises coastal plains of up to 160 km width in the north, which narrow to less than 40 km and then slightly widen again in the south (Suárez et al., 1983). The N-S-trending Chilean segment of the coastal region includes the up to 2,700-m-high Coastal Cordillera, which decreases in altitude to 500 m at 46°S (Jordan et al., 1983).

Multiple marine terraces, at successively higher elevations, are formed along the forearc coast at glacial-cycle time scales through the combined effects of wave erosion, tectonic uplift, and climate-driven sea-level oscillations. Interglacial and interstadial relative sea-level highstands during Pleistocene warm periods were responsible for the carving of abrasion platforms and the retreat of coastal cliffs, which were subsequently exposed due to continued uplift and a falling sea level during cold periods. If the coastal uplift rate in such a scenario is
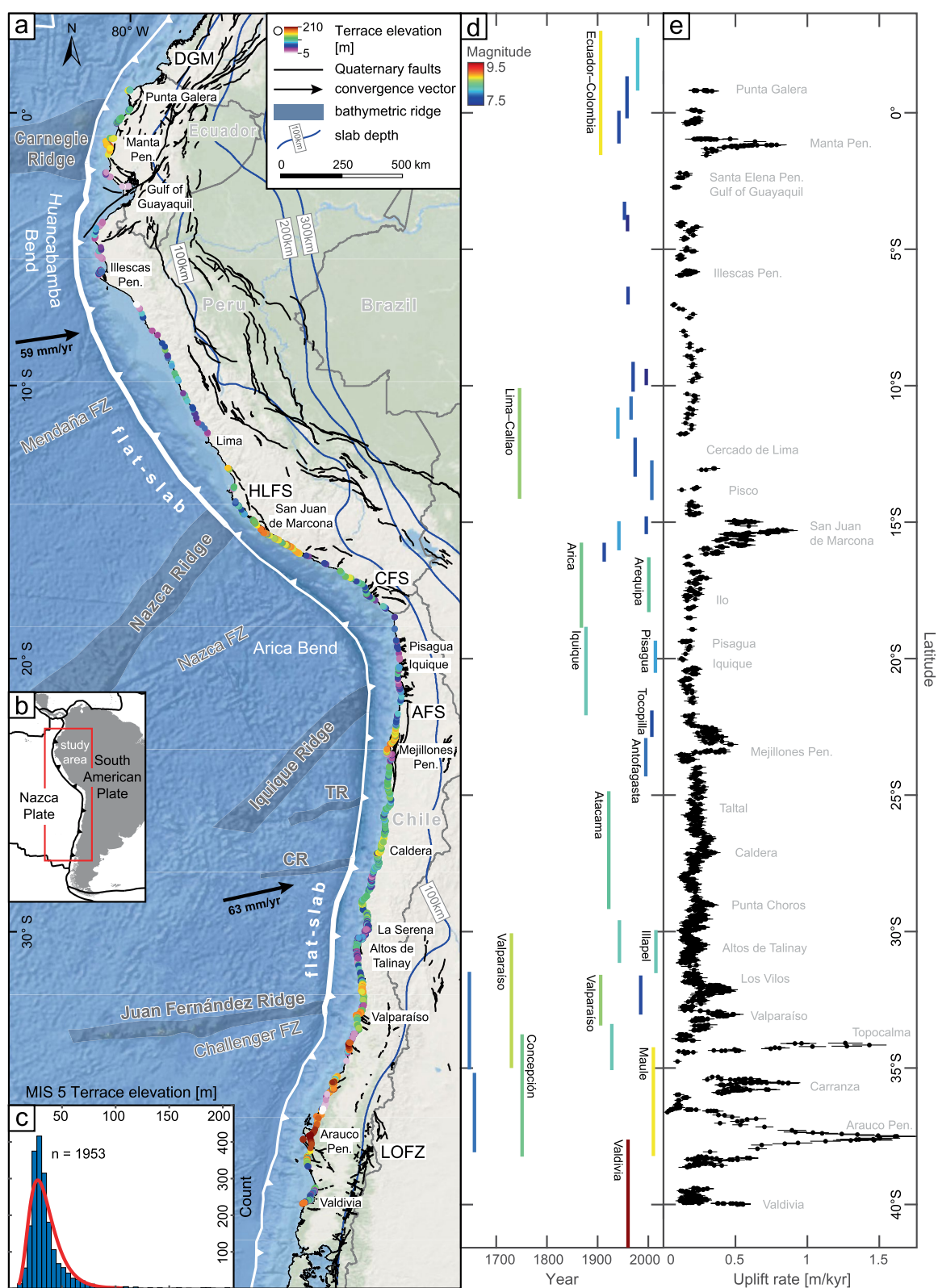
Figure 1.

sufficiently high, the abrasion platforms will remain subaerially exposed; during the following relative sea-level highstand, a new abrasion platform will be sculpted into the rocks of the forearc at a lower position, thus leading to a staircase morphology (e.g., Lajoie, 1986). The resulting terrace sequences are assigned to odd-numbered Marine Isotope Stages (MIS; Shackleton et al., 2003). Multiple marine terrace levels can be observed along almost the entire western coast of South America. Based on global observations of sea-level fluctuations, the surface of the last-interglacial marine terrace (MIS 5) is associated with three second-order highstands; these comprise MIS 5a at 80 kyr, MIS 5c at 105 kyr, and MIS 5e at ∼125 kyr (from 128 to 116 kyr), associated with paleo-sea levels at −20 ± 5 m for both of the younger and +3 ± 3 m for the oldest highstand (Hearty et al., 2007; Pedoja et al., 2011; Rohling et al., 2009; Siddall et al., 2006; Stirling et al., 1998). The best-preserved and laterally most continuous terrace level was formed during MIS 5e and has been used frequently as a geomorphic strain marker for the estimation of coastal deformation and uplift rates, both in South America and elsewhere (Dumas et al., 2006; Freisleben et al., 2021; Jara-Muñoz et al., 2015; Matsu'ura et al., 2019; Muhs et al., 2002, 2014; Saillard et al., 2011; Simms et al., 2020; Tam & Yokoyama, 2021).

2.2. Subduction Geometry and Bathymetry of the Subducting Plate

At the convergent margin of South America, the oceanic Nazca Plate subducts beneath the South American continent with fairly constant convergence rates, varying between 59 mm/yr in the north (8°S) and 63 mm/yr in the south (27°S), as well as convergence azimuths, varying from N84.1° in the north to N80.7° in the south (Figure 1; Kendrick et al., 2003). The subduction zone in South America can be divided into four major segments based on spatial distributions of Benioff-zone seismicity, which delineate varying angles of the subducting slab (Figure 1). Relatively steep segments of the subducting plate, dipping 25°–30° at depths of ∼100 km, are interrupted by two major flat-slab subduction segments, dipping only 5°–10°, beneath central Peru (2°–15°S) and central Chile (27°–33°S), respectively (Hayes et al., 2018; Jordan et al., 1983).

Several bathymetric anomalies characterize the seafloor of the subducting plate, the two most prominent ones being the Carnegie and Nazca aseismic ridges at 0° and 15°S, respectively. The 300-km-wide and ∼2-km-high Carnegie Ridge subducts roughly parallel to the convergence direction, while the obliquity of the 200-km-wide and 1.5-km-high Nazca Ridge has caused its intersection with the trench to be shifted 500 km toward the SE during the last 10 Ma (Gutscher et al., 1999; Hampel, 2002; Kendrick et al., 2003). Additional smaller bathymetric anomalies include the Juan Fernández, Copiapó, Taltal, and Iquique ridges, as well as several fracture zones (e.g., Mendaña and Nazca fracture zones; Figure 1a). The subduction of these bathymetric anomalies influences the degree of interplate coupling and the associated seismic hazard by creating fracture networks that promote small earthquakes and aseismic creep (Bassett & Watts, 2015; Collot et al., 2017; Wang & Bilek, 2011).

2.3. Major Coastal Fault Systems and Seismicity

The main structures affecting the convergent margin of the western South American coast comprise multiple fault systems with varying kinematics; their occurrence is closely connected with the subducting Nazca Plate and inherited heterogeneities in the South American continental plate (e.g., Armijo & Thiele, 1990; Audin et al., 2008; Wang & Bilek, 2014). North of the Huancabamba Bend, dextral strike-slip and thrust faulting occurs in the coastal areas of Ecuador, although normal faulting has been observed at some locations such as Punta Galera or at the Manta Peninsula (Figure 1). The largest structure in this region is the 2,000-km-long, dextral and NE-striking DGM, which separates the northern from the southern forearc units and is associated with normal faulting in the Gulf of Guayaquil, as well as dextral strike-slip faulting on the Santa Elena Peninsula and regions to the north (Alvarado et al., 2016; Baize et al., 2015; Margirier et al., 2023). In the coastal regions of Peru, normal faulting occurs primarily on the Illescas Peninsula, within the El Huevo-Lomas fault system

Figure 1. (a) Tectonic setting of the western South American plate margin showing the major crustal fault systems (Costa et al., 2000; Maldonado et al., 2021; Veloza et al., 2012), slab depth (Hayes et al., 2018) and flat-slab subduction segments, bathymetric features of the subducting plate, convergence vectors (Kendrick et al., 2003), and elevations of last-interglacial marine terraces (Freisleben et al., 2021) DGM, Dolores-Guayaquil Megashear; HLFS, El Huevo-Lomas fault system; CFS, Chololo fault system; AFS, Atacama fault system; LOFZ, Liquiñe-Ofqui fault zone; FZ, fracture zone; TR, Taltal Ridge; CR, Copiapó Ridge (World Ocean Basemap: Esri, Garmin, GEBCO, NOAA, NGDC, and other contributors). (b) Location of the study area. (c) Histogram of last-interglacial marine terrace elevations from the database of Freisleben et al. (2021). The count of terrace elevations follows a log-normal distribution with a median of 30 m. MIS 5, Marine Isotopic Stage 5. (d) Latitudinal extent of great subduction earthquakes (≥M7.5) along the western South American coast between 1647 and 2015 colored by magnitude (Udias et al., 2012; Villegas-Lanza et al., 2016) (e) Uplift rates of last-interglacial marine terraces (MIS 5e and 5c) calculated from the terrace elevations of Freisleben et al. (2021).

(San Juan de Marcona area), and within the Chololo fault system (CFS) farther south (Audin et al., 2008; Costa et al., 2020; Veloza et al., 2012). The principal coastal faults that have been described along the northern Chilean convergent margin are part of the Atacama fault system (AFS), which extends from Iquique to La Serena (30°S) with predominantly N-S-striking normal faults (Figure 1; Naranjo, 1987; Santibáñez et al., 2019). Smaller and more disconnected fault systems occur farther south in the Altos de Talinay area (e.g., Puerto Aldea fault) near Valparaiso, Topocalma, and Carranza, and on the Arauco Peninsula (Figure 1; Maldonado et al., 2021).

Most great (≥M_W7.5) earthquakes along the tectonically active western margin of South America are associated with the subduction of the Nazca Plate beneath the South American continent, although some correspond to normal-faulting events within the down-going slab (Beck et al., 1998). Figure 1d shows the spatial and temporal distribution of those earthquakes, which display patterns of recurrent great events in distinct seismotectonic segments of the forearc (Lomnitz, 2004; Molina et al., 2021; Saillard et al., 2017).

3. Methods and Data

Our approach to analyze the terrace signal and potential processes controlling the spatial distribution of uplift rates comprises the decomposition of the signals themselves and a comparison of their wavelength spectra. The calculations and outputs were processed and elaborated using MATLAB®. Although various approaches have been used at a continental scale to unravel processes responsible for the accumulation of permanent deformation in the forearc (e.g., Malatesta et al., 2021; Rousset et al., 2016), our approach is specifically targeted toward a comparison of wavelengths of long-term uplift rates with potential processes and conditions that generate specific deformation signals. We used uplift rates calculated from the terrace-elevation database of Freisleben et al. (2021). We are aware that terrace-elevation measurements within the database vary in quality based on several factors, most notably the distance to the nearest age estimate. However, the continuous distribution and generally good quality rating of the measurements (Freisleben et al., 2021) provide the unique opportunity to thoroughly analyze this database for the first time on a continent-wide scale, and to compare it with potential parameters and associated mechanisms that may influence permanent forearc deformation along the coast. Sensitivity tests on the wavelength analysis using only points above a certain quality-rating threshold did not reveal any significant changes in comparison with the entire database (Figure S7 in Supporting Information S1).

3.1. Input Signals

For the marine terrace signal, we calculated uplift rates using MIS 5e and 5c shoreline-angle elevations of last-interglacial marine terraces (Freisleben et al., 2021) together with associated sea-level altitudes and terrace-age estimates. We analyzed and compared the dominant wavelengths of the marine terrace signal to those of the signals of residual gravity anomaly, interseismic uplift rate, effective basal friction, coseismic land-level change, bathymetric anomaly, distance to the trench, and background seismicity (Figure 2). To allow for a better comparison with terrace-uplift rates, we extracted all signals except bathymetric anomaly and background seismicity at the terrace locations and projected them along the trench.

The signal of residual gravity anomaly was obtained by applying the principal component analysis method, described in Molina et al. (2021) for the Chilean margin, to the Free-Air gravity anomaly grid from Sandwell et al. (2014) for the entire western coast of South America (Figure S1a in Supporting Information S1). In a second step, we calculated the mean value along trench-perpendicular profiles from the terrace location to the trench. This latter value provides an indirect measure of the effective normal stress across the entire accretionary wedge, since the residual gravity anomaly is associated with variations in forearc density and thus vertical stresses acting on the megathrust (Molina et al., 2021). To attain estimates of interseismic uplift rate, we used the block model of Graham et al. (2018; modified for South America), which decomposes interseismic GPS velocities to slip deficit on block-bounding faults, coupling on triangular dislocation elements (Figure S1b in Supporting Information S1), and plate rotations. We then calculated interseismic uplift rates at the terrace locations using the results of the block model and a built-in forward-model function. For the signal related to great subduction earthquakes, we used Okada models of 12 great earthquakes (≥M_W7.5) since 1995 that were generated from finite fault models by Hayes (2017) (Figure S1c in Supporting Information S1). We extracted the cumulative vertical displacement at the location of each marine terrace measurement from these models to create a signal of coseismic land-level changes along the South American coast. To obtain the signal related to bathy-

metric anomalies, we generated a 150-km-wide, trench-parallel swath profile west of the trench, on which we subsequently applied a high-pass Butterworth filter (Figure S9 in Supporting Information S1). This filter served to generate a signal of bathymetric irregularities instead of bathymetric depth, by enhancing high-frequency parts of the bathymetry signal while maintaining the long wavelengths. We estimated the distance to the trench by projecting the points of the marine terrace measurements perpendicular to the trench and using the obtained projection distance.

Another parameter included in our analysis was the coefficient of effective basal friction (μ_b^{eff}). Assuming the forearc acts like a noncohesive critical Coulomb wedge, the critical taper angle can be described by its coefficients of internal and basal friction (μ_i and μ_b) as well as its internal and basal Hubbert-Rubey fluid-pressure ratios (λ_i and λ_b) (Dahlen, 1984). To calculate μ_b^{eff}, we used a combination of the solution for a noncohesive critical Coulomb wedge by Dahlen (1984) generalized with a Mohr's construction by Lehner (1986), which was established by Cubas et al. (2013)

$$\mu_b^{eff} = (1 - \lambda_b)\, \mu_b \tag{1}$$

The critical taper angle $(\alpha + \beta)_{crit.}$ is calculated using the angles between the maximum principal stress and the base and the top of the wedge (ψ_b and ψ_0)

$$(\alpha + \beta)_{crit.} = \psi_b - \psi_0 \tag{2}$$

where the two angles ψ_b and ψ_0 are a function of the internal and basal angles of friction (ϕ_i and ϕ_b)

$$\psi_b = \frac{1}{2}\arcsin\left(\frac{\sin \phi_b'}{\sin \phi_b}\right) - \frac{1}{2}\phi_b' \text{ with } \mu_b = \tan \varphi_b \text{ and} \tag{3}$$

$$\psi_0 = \frac{1}{2}\arcsin\left(\frac{\sin \alpha'}{\sin \phi_i}\right) - \frac{1}{2}\alpha' \text{ with } \mu_i = \tan \varphi_i \tag{4}$$

The angles α' and ϕ_b' additionally take into account pore-fluid pressure through internal and basal Hubbert-Rubey fluid-pressure ratios

$$\tan \phi_b' = \left(\frac{1 - \lambda_b}{1 - \lambda_i}\right)\tan \phi_b \tag{5}$$

$$\alpha' = \arctan\left[\left(\frac{1 - \frac{\rho_w}{\rho}}{1 - \lambda_i}\right)\tan \alpha\right] \tag{6}$$

To calculate the topographic slope (α), we divided the height difference between the trench and the terrace location by their distance using the GEBCO 2020 bathymetric and topographic grid (GEBCO Bathymetric Compilation Group, 2020). The dip of the subducting plate (β) is derived from the slab depth at the terrace location, using the Slab2.0 model of Hayes et al. (2018), and the distance to the trench. For the remaining coefficients we chose $\mu_i = 0.6$, $\lambda_i = \lambda_b = 0.85$, $\rho = 2.7$ g/cm^3, $\rho_w = 1$ g/cm^3, where ρ and ρ_w are the densities of the wedge material and the pore fluid (water), respectively. The chosen values for μ_i and λ_i are commonly used values for the coefficient of internal friction in South America and the pore-fluid-pressure ratio according to Byerlee's law (Cubas et al., 2013; Dahlen, 1984).

Background seismicity constitutes the last continuous signal that we analyzed and compared with the uplift rate. We extracted background seismicity along the western South American coast following the approach of Madella and Ehlers (2021), using all earthquakes that occurred since 1973 between the trench and the 60-km depth contour from the USGS earthquake catalog; prior to 1973, the records are incomplete (https://earthquake.usgs.gov/earthquakes/search/, downloaded on 17.09.2021). Additional filters include a reduction of the magnitude range (M4.3–M6) based on a Gutenberg-Richter plot. In addition to using all of the described seismic events in one analysis (Figure S3 in Supporting Information S1), in a separate analysis (Figure S4 in Supporting Information S1) we excluded earthquakes >10 km away from the subducting slab. To retrieve the background seismicity, we excluded great earthquakes with multiple postseismic events by carrying out a cluster analysis, using the DBSCAN algorithm in MATLAB® based on spatial and temporal cluster characteristics. We then counted

Table 1
Fault Parameters Used for Elastic Modeling of Crustal Faults

Model run	Up-dip depth (km)	Down-dip depth (km)	Dip	Slip rate (mm/yr)	Rake
1–3	0	25	60	0.2; 1;2	90
4–6	2	25	60	0.2; 1;2	90
7–9	0	15	60	0.2; 1;2	90
10–12	0	25	90	0.2; 1;2	90

Note. Up-dip depth, down-dip depth, or fault dip change after three model runs, during which three different slip rates are tested.

all earthquakes within 20-km-wide bins from the subduction trench to the 60-km depth contour to obtain a signal for background seismicity (Figures S3 and S4 in Supporting Information S1).

3.2. Signal Analysis

The signal analysis involved several steps to estimate the contribution of each process influencing the observed signal of cumulative permanent coastal uplift. In an initial step, we interpolated the signals using a step size of 10 km to ensure equal point density along the entire length of the trench (see Figure S11 in Supporting Information S1 for point spacing before interpolation). To assess the role of the step size for the interpolation of input signals, we carried out a sensitivity test, which showed no significant change of the output wavelength spectrum for step sizes ≤30 km (Figure S6 in Supporting Information S1). In a second step, we carried out an FFT and calculated the power spectral density (PSD) of the frequency range for each signal, which we reciprocated to obtain wavelength values. By the application of an inverse FFT and a power-spectrum threshold below the major peaks we were able to accurately reproduce the input signals.

Spectral comparison of uplift rates and tectonic parameters via signal analysis focuses on the distribution of wavelengths but neglects the equally important aspect of spatial coherence between individual signals. However, we propose that this kind of analysis accounts for spatiotemporal changes in tectonic processes over millennial time scales that might otherwise be overlooked.

Apart from these continuous signals along the margin, we also analyzed wavelengths related to discrete processes such as crustal faulting, which, although not suitable for FFT, might still control parts of the uplift-rate spectrum. We analyzed crustal faulting using Okada models (Okada, 1992) of 33 faults near the coast with the input fault geometry and fault parameters of the CHAF database of active faults in Chile (Figures S2 and S8 in Supporting Information S1; Maldonado et al., 2021). Since the depth, dip, slip rate, and rake are not well known for most of the analyzed faults, we iterated several dislocation models by arbitrarily varying these parameters within defined ranges based on well-studied faults in South America of similar kinematics (Table 1).

We used a down-dip depth of 25 km for the elastic models, which is typical for crustal faults in the coastal forearc (e.g., El Yolki Fault in Melnick et al. (2019)), changing this parameter only for three model runs to a depth of 15 km (e.g., Santa María Fault in Jara-Muñoz et al. (2017)). From the Okada models, we extracted displacement profiles of 200-km length perpendicular to the fault strike and calculated the distance between −10 and 10 cm displacement (Figure S8 in Supporting Information S1). The resulting lengths are displayed in a histogram and are fitted to a kernel-density function (Figure 4).

3.3. Estimation of Spectral Correlation

We quantified correlations between uplift rate and the analyzed tectonic features using the resulting wavelength spectra. To ensure equal point spacing and similar maximum amplitudes, we interpolated (step size: 10 km) and normalized all wavelength signals. Since most of the analyzed features are restricted to specific wavelength ranges, we calculated the product of normalized PSDs of tectonic parameters and uplift rate for each wavelength point to quantify and locate high correlation with respect to the uplift-rate spectrum (Figures 5 and Figures S12–S19 in Supporting Information S1). The linear correlation coefficients between the entire spectra were also included in our calculations.
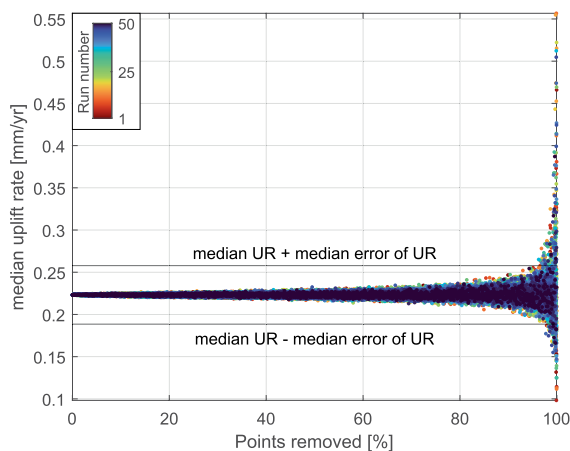
4. Results

For the description of the wavelength analysis, we defined three categories of peaks depending on their amplitude relative to the maximum amplitude of the wavelength spectrum. Wavelength peaks are considered small, medium, or large if they reach <30%, 30%–60%, or >60% of the maximum amplitude, respectively.
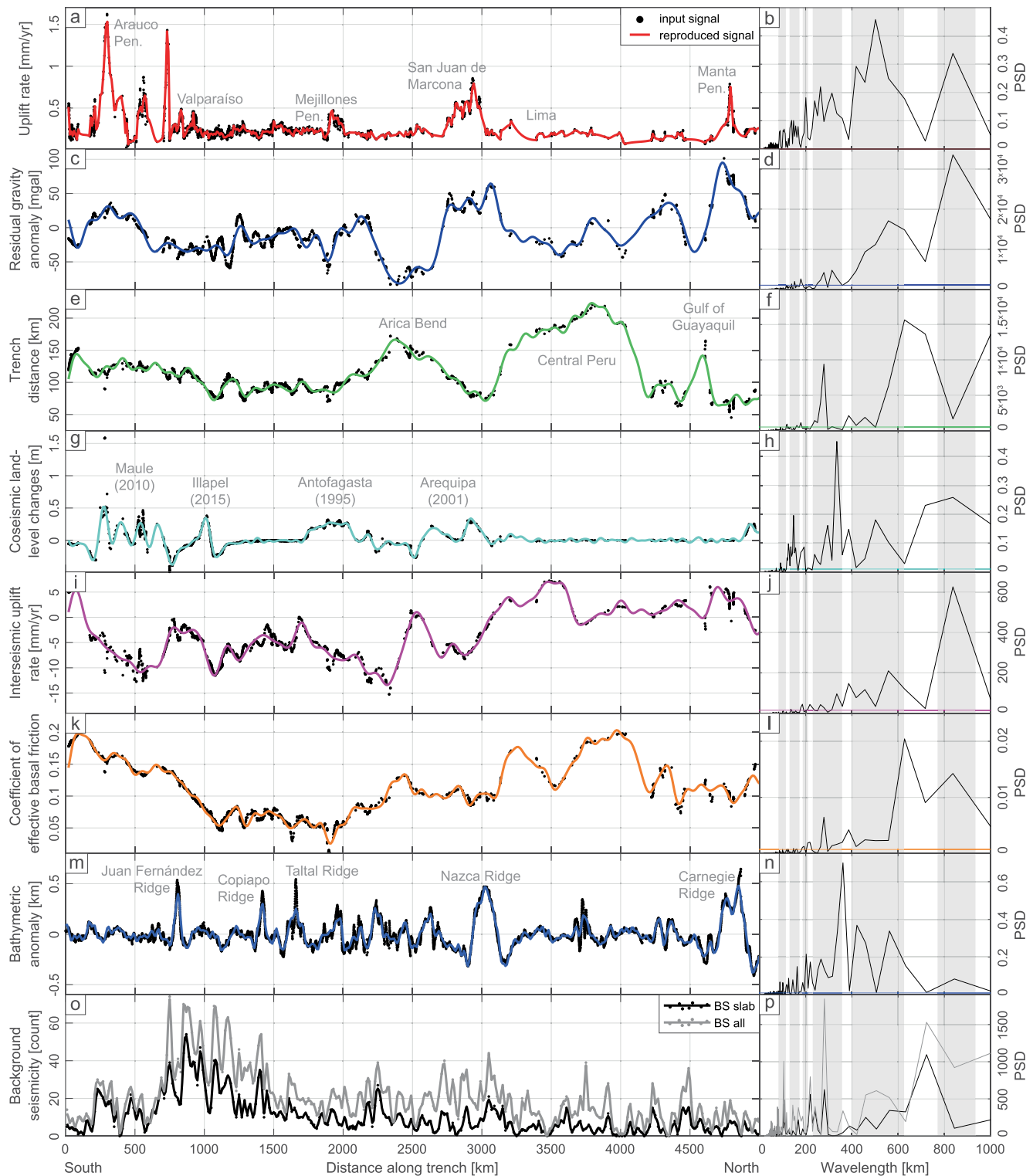
Figure 2. Comparison of the uplift-rate signal (a) and its corresponding wavelength spectrum (b) with the signals and analysis of various tectonic parameters including residual gravity anomaly (c, d), distance to the trench (e, f), coseismic land-level changes (g, h), interseismic uplift rate (i, j), effective basal friction (k, l), bathymetric anomaly (m, n), and background seismicity (o, p). Vertical gray bars in the wavelength spectra indicate the most prominent peaks in the uplift-rate range. Orientation: South-North.
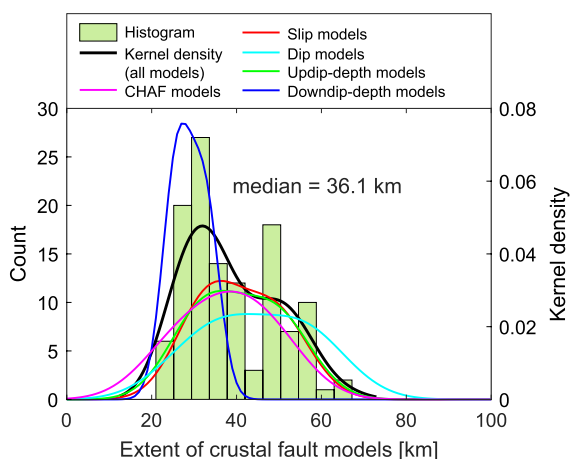
4.1. Uplift-Rate Signal

At the scale of the western coast of South America, long-term coastal uplift rates estimated over the past ~125 kyr display a relatively constant background signal (median: 0.225 mm/yr) with at least 10 short-wavelength (e.g., near Los Vilos, Valparaíso, Carranza) and five long-wavelength peaks (e.g., on the Manta and Arauco peninsulas, San Juan de Marcona; Figure 2a). To test the reliability of the background signal, we randomly removed an increasing number of uplift-rate estimates from the terrace database while calculating the median of the remaining values. We iterated this procedure 50 times to eliminate any statistical artifacts for the randomly removed points. We only observed a significant variation of the median uplift rate (deviating more than the median error of uplift rate) when >90% of the points were removed (Figure 3). We therefore consider the background signal of uplift rate to be significant at the scale of the South American margin.

The wavelength spectrum of the uplift-rate signal resulting from the FFT analysis shows several small peaks at wavelengths between 20 and 180 km, medium peaks within the range of 190 and 360 km, a broad large peak between 400-km and 600-km wavelength, and another large peak at 835 km (Figure 2b).

4.2. Residual Gravity Anomaly and Distance to the Trench

The residual gravity anomaly along the western coast of South America varies between −100 and 100 mgal, showing a relatively long-wavelength signal (Figure 2c). The wavelength spectrum indicates only a few small peaks below 400 km. The main part of the signal is characterized by a broad medium-sized peak between 430-km and 650-km wavelength and a major peak at 835 km (Figure 2d). Only two smaller peaks appear at wavelengths of 280 and 310 km.

The distances from our terrace-measurement locations to the trench vary between 50 and 150 km but show large and very long-wavelength increases (>1,000 km) at the Arica Bend in Chile and in central Peru (Figure 2e). Shorter-wavelength changes in distance to the trench are represented in the wavelength spectrum by two large peaks at 280 km and between 580-km and 750-km wavelength (Figure 2f).

4.3. Coseismic Land-Level Changes and Interseismic Uplift Rate

Coseismic vertical displacements show an even distribution of subsidence and uplift along the coast (Figure 2g and Figure S10 in Supporting Information S1), with most significant land-level changes resulting from the Illapel (2015), Maule (2010), Arequipa (2001), and Antofagasta (1995) earthquakes. The wavelength spectrum displays three small peaks (at 125, 195, and 240 km), five medium peaks (at 150, 295, 385, 500, and 780 km), and one large peak (at 335 km) representing mainly intermediate to long-wavelength signals (Figure 2h).

The signal of interseismic vertical velocities is characterized by medium to long wavelengths, indicating subsidence in Chile/southern Peru and uplift primarily in northern Peru/Ecuador (Figure 2i). The wavelengths might result partially from the model resolution, which is constrained by a triangular-element raster with side lengths between ~60 and 100 km (Graham et al., 2018). We observe multiple small peaks in the spectrum below 500-km

Figure 3. Reliability test of the continuous background signal of uplift rates. Median uplift rates (*y*-axis) stay relatively constant when an increasing number of terrace measurements is removed (*x*-axis). The different colors display the individual runs of random point removal ($n = 50$), and the black horizontal lines represent the median uplift rate plus or minus the median error of uplift rate.

Figure 4. Histogram of the extent of fault displacement resulting from all elastic Okada models with either CHAF parameters or varying fault parameters for less well-studied crustal faults. Colored graphs represent kernel-density functions of the individual fault models, where the specified parameter changes according to Table 1; bold black line represents the kernel fit for all Okada models.

wavelength, while one medium peak appears at 560-km wavelength and one large peak can be observed at 835 km (Figure 2j).

4.4. Basal Friction and Bathymetric Anomalies

Along the western coast of South America, effective basal friction varies in a long-wavelength pattern from ∼0 to 0.2, with higher values characteristic for Peru and south-central Chile (Figure 2k). Analysis of this signal reveals two small peaks around 200 km and one at 390 km, a medium peak at 280-km wavelength, and two large peaks at 630 and 835 km (Figure 2l).

The filtered and detrended bathymetry signal that represents bathymetric anomalies shows changes of ±500 m, with the most significant anomalies at the Nazca, Carnegie, Juan Fernández, Copiapo, and Taltal ridges (Figure 2m). This signal results in a power spectrum with three small peaks from 165-km to 265-km wavelengths and at 845 km, two medium peaks at 440 and 560 km, and one large peak at 360-km wavelength (Figure 2n).

4.5. Background Seismicity and Crustal Faulting

The signal of background seismicity shows relatively low variability with seismicity increasing broadly (hundreds of km width) in the vicinity of the Juan Fernández Ridge (Figure 2o). Accordingly, the wavelength spectrum shows several small peaks below 240 km and two medium peaks at 105 and 220 km (Figure 2p). We further observe a medium to large peak at 280 km, a broad medium-sized peak from 450 to 600 km (only for the entire background-seismicity signal), and another large peak at 720-km wavelength.

We performed 120 elastic Okada models on 33 crustal faults along the western South American coast, which show absolute vertical displacements (>10 cm) in areas of maximum 22.5–66.2 km extent measured perpendicular to the fault trace (Figure 4 and Figure S8 in Supporting Information S1). The kernel-fitted density function of this wavelength distribution shows an asymmetric peak at smaller wavelengths with a median at 36.1 km (Figure 4).

5. Discussion

5.1. Processes Controlling Various Wavelengths of Deformation

The mechanisms contributing to the accumulation of permanent deformation along tectonically active forearcs are currently a matter of debate, primarily because they have not yet been analyzed on a continental scale (Jolivet et al., 2020; Mann et al., 1998; Melnick, 2016; Menant et al., 2020). We attempt to contribute to this ongoing debate by analyzing and comparing the wavelength signal of terrace-uplift rates with the wavelength signals of a selection of tectonic parameters thought to be associated with processes causing permanent forearc uplift at the coast. For better comparability, we divided the uplift-rate spectrum in ranges of short-wavelength (<100 km), intermediate-wavelength (100–450 km), and long-wavelength (>450 km) deformation. Although our analysis reveals multiple patterns and parameters correlating to certain ranges of wavelength in the uplift-rate spectrum, we infer that a specific set of processes associated with the seismotectonic segmentation of the megathrust is responsible for these signals (Figure 5). Although a correlation is not proof of a causal relationship, multiple correlations of different tectonic mechanisms and parameters can be inferred to support a specific potential mechanism, especially when the parameters are independent of each other. Furthermore, we attempted to correlate mechanisms that have been previously proposed as drivers of coastal uplift and use these correlations to test hypotheses.

Linear correlations between the entire wavelength spectra of coastal uplift rate and potential driving mechanisms are highest for the residual gravity anomaly and interseismic uplift rate, and to a lesser extent for coseismic land-level changes and bathymetric anomalies, suggesting that these phenomena are characterized by similar wavelengths as the long-term uplift-rate pattern (Figure 5). In contrast, the negative correlations of background seismicity, trench distance, and crustal faulting are attributed to the dominance of certain wavelengths in these spectra that are not present or not as pronounced in the long-term uplift-rate signal.
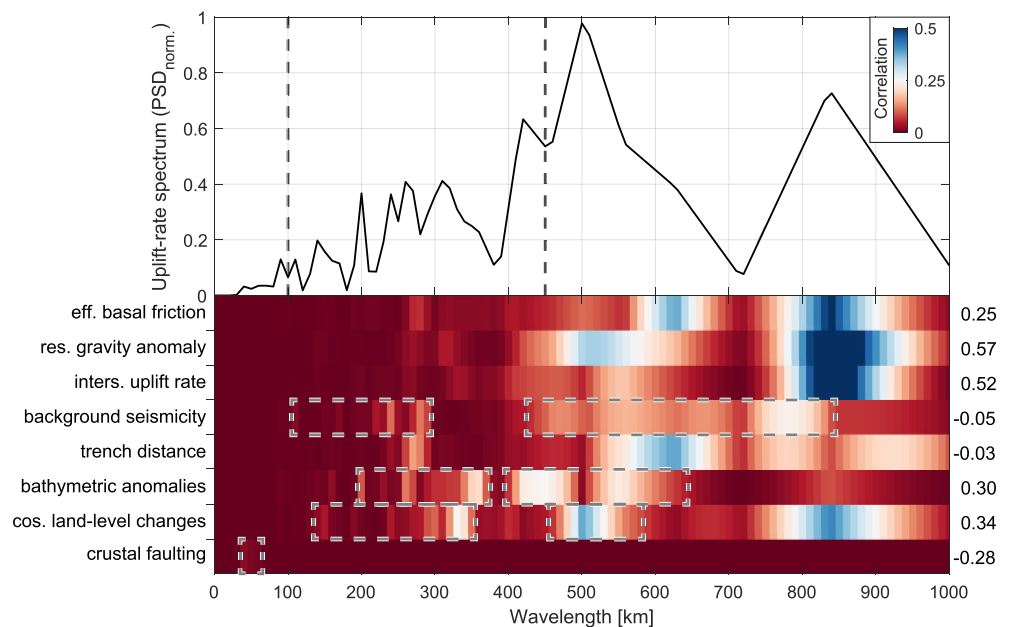
Figure 5. Normalized wavelength spectrum resulting from the analysis of the uplift-rate signal (top). Dashed black lines indicate ranges of short-wavelength (<100 km), intermediate-wavelength (100–450 km), and long-wavelength (>450 km) deformation. Color scales below quantify and localize the correlation (0—red to 0.5—blue) between the wavelength spectra of the tectonic parameters and the uplift rate. Gray dashed boxes indicate several correlations described in the text, and the numbers on the right quantify the linear correlation between the full spectra.

Quantifying and localizing correlations at specific wavelengths suggest that short wavelengths (<100 km) in the uplift-rate signal are mainly caused by crustal faulting, as might be expected. The absence of a significant overall correlation between uplift rate and crustal faulting is attributed to the low power of short-wavelength signals in the uplift-rate spectrum. However, we consider wavelengths between 22.5 and 66.2 km to be a reasonable maximum estimate for the wavelength of uplift signals controlled by crustal faults (Figure 4), taking into account that small faults may be underrepresented in our analysis and that complete rupture of large faults is rare. Intermediate-wavelength (100–450 km) variations in terrace-uplift rate coincide in the spectrum primarily with (a) coseismic vertical displacements related to great earthquakes (M7.5–M8), (b) medium bathymetric anomalies (e.g., Taltal or Copiapo ridges), and (c) high-frequency changes in background seismicity (Figure 5). The correlating shorter wavelengths of these features may indicate the locked areas on the megathrust, which rupture either during multiple small cascading events (background seismicity) or during great earthquakes (Madella & Ehlers, 2021; Métois et al., 2016; Remy et al., 2016; Schurr et al., 2014). The respective longer wavelengths (megathrust earthquakes > M8, long-wavelength background seismicity, large bathymetric anomalies) are similarly correlated with the uplift-rate spectrum in the long-wavelength range (>450 km) and might represent the upper extent of locked megathrust patches. The remaining parameters primarily show correlations with the uplift-rate spectrum at long wavelengths, namely interseismic uplift rates, basal friction, residual gravity anomaly, and to a lesser extent trench distance (Figure 5). However, we note that the distance to the trench is included in the calculation of effective basal friction and is therefore not independent from this parameter. The related processes might influence the long-term seismotectonic segmentation of the megathrust on 10^2-km scales and affect the physical behavior of the megathrust. This may apply, for instance, to lateral density variations in the forearc that change the vertical loading on faults and thus the effective normal stresses (Cubas et al., 2013; Molina et al., 2021).

Our signal-analysis approach supports the notion that mechanisms such as the subduction of bathymetric anomalies and coseismic slip are related to various wavelengths of permanent deformation and the seismotectonic segmentation of the megathrust, as had been proposed in previous studies (Molina et al., 2021; Philibosian & Meltzner, 2020; Singh et al., 2011). In light of this finding, we emphasize the significant correlations between terrace-uplift rates and coseismic land-level changes in both long-wavelength and intermediate-wavelength ranges, suggesting primarily coseismic accumulation of permanent coastal uplift (Figure 5; González-Alfaro

et al., 2018; Melnick, 2016). Our analysis furthermore confirms that short-wavelength deformation in the coastal forearc is controlled by crustal faults in the upper plate (Jara-Muñoz et al., 2015; Kelsey et al., 1996; Matsu'ura, 2015), while long-wavelength parameters such as basal friction or residual gravity anomalies might influence the larger-scale segmentation of the megathrust (Molina et al., 2021). Our results underscore that the signal of uplift rates averaged since the last interglacial along the South American margin is controlled by processes acting on different time scales and originating from deep-seated regional as well as crustal local sources, as has been suggested for other subduction margins (e.g., Ferranti et al., 2006, 2010).

5.2. The Continuous Uplift-Rate Signal Along the Western Coast of South America

Besides the previously described and interpreted deformation patterns with wavelengths of up to 850 km, we observe a fairly continuous background signal of uplift rate along the entire western South American margin (Figures 1e and 3), which may be explained by two potential scenarios. In the first scenario, the background uplift could originate from a single, low-magnitude mechanism acting continuously along the entire margin. The second scenario involves a single or multiple, spatially distributed processes that temporarily change location and/or magnitude and accrue over millennial time scales toward a continuous and permanent signal of background-uplift rate. In search for the mechanism(s) responsible for the observed background-uplift-rate signal, we exclude processes that have a localized and high-amplitude impact on the comparatively low-amplitude, continuous signal of background-uplift rate. These include phenomena attributed to the subduction of bathymetric anomalies, such as high-uplift areas where the Nazca and Carnegie ridges intercept the forearc (e.g., Hsu, 1992; Pedoja et al., 2006), the coastal sectors of Topocalma, Carranza, and Mejillones with pronounced crustal faulting, or the Arauco peninsula characterized by the motion of a forearc sliver (Jara-Muñoz et al., 2015; Melnick et al., 2009). Such processes have also been associated with short-wavelength to intermediate wavelength of upper-plate deformation at other subduction zones (Gardner et al., 2013; Kelsey et al., 1996; Matsu'ura, 2015; McKenzie et al., 2022; Sak et al., 2004) and are viewed as unlikely to accommodate a continuous low-magnitude background-uplift rate as observed by us.

With respect to the first scenario of a single, low-magnitude mechanism acting continuously along the entire margin, the low-magnitude mechanisms and parameters generally seem to lack the spatial continuity that would be required to explain the observations. Background seismicity (Figure 2o) could be considered for this scenario, since Madella and Ehlers (2021) show a possible correlation with long-term uplift rates in northern Japan and central South America. However, high-frequency changes in the inferred signal of background seismicity and the relatively short time interval of ∼50 years analyzed in comparison with the duration of a seismic cycle (∼100–300 years; Cisternas et al., 2005; Comte & Pardo, 1991) prevent further interpretations regarding the role of this mechanism.

Alternatively, the virtually continuous background signal of uplift rates might result from a single or various mechanisms of different wavelength, timing, and location that overlap and accumulate over millennial time scales. We used the results of our analysis to test the mechanism proposed by Jolivet et al. (2020), who suggest that a small portion of interseismic uplift translates into permanent deformation. We also tested the hypothesis put forward by Melnick (2016), who suggested major, domain-C earthquakes (∼35–55-km depth) to be responsible for permanent coastal uplift signals. Based on the depth zonation suggested by Lay et al. (2012), such domain-C earthquakes are characterized by smaller, isolated megathrust patches that usually cause great-sized events.

The mechanism proposed by Jolivet et al. (2020) was tested by plotting analyzing two different plots of interseismic uplift rates against terrace-uplift rates, one excluding the points in the vicinity of crustal faults and the other including only such points. The selection of fault-influenced points was made using a 10-km-wide buffer around each coastal fault from the CHAF and GEM databases (Maldonado et al., 2021; Styron & Pagani, 2020). Interestingly, interseismic uplift displays no direct correlation with terrace-uplift rates, neither when points near active faults are removed (Figure 6a), nor when only points in the vicinity of crustal faults are plotted (Figure 6b). Furthermore, interseismic velocities indicate almost exclusively subsidence for southern Peru and Chile, representing ∼60% of the analyzed margin (Figure 2i), whereas the terrace record only records long-term uplift. On the other hand, testing such a relationship at a continental scale cannot rule out local, smaller-scale correlations between interseismic and long-term coastal uplift. We therefore suggest that either a very small fraction of interseismic slip is being accumulated as permanent deformation or that such a mechanism is confined to specific local areas.
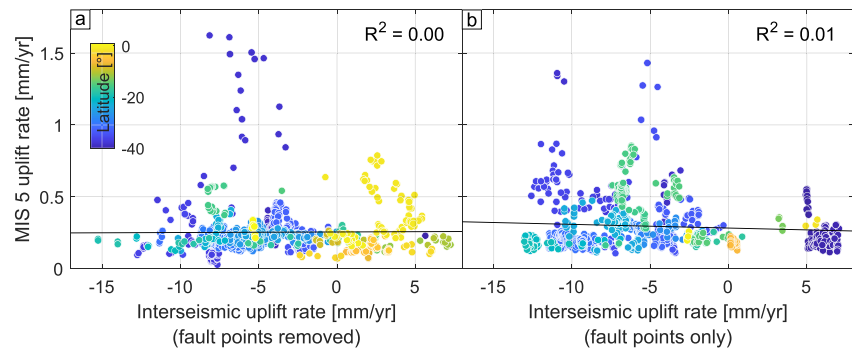
Figure 6. Interseismic uplift rates derived from the block model show no correlation with long-term uplift-rate estimates of marine terraces. (a) Points >10 km away from active faults and (b) points ≤10 km away from active faults based on the CHAF and GEM databases (Maldonado et al., 2021; Styron & Pagani, 2020). All points are colored by latitude.

Since the occurrence of great earthquakes ($M > 7.5$) exhibits an equal degree of coseismic coastal subsidence and uplift (Figure 2g and Figure S10 in Supporting Information S1; Gusman et al., 2015; Melnick, 2016; Ocola, 2008), we infer no generally applicable and immediate causality between coseismic vertical displacements and terrace-uplift rates. Apparently, not all earthquakes are responsible for permanent coastal uplift, but major earthquakes near the Moho (domain-C earthquakes: ~35–55-km depth; M7–M8) that have recently caused several decimeters of coastal uplift (Figures 7a and 7b) might explain the observed background-uplift rates. The well-correlated wavelength spectra of terrace-uplift rate and coseismic coastal uplift resulting from such events (Figure 7c) indicate the relationship between both features. In conjunction with moderate coseismic uplift resulting from major, domain-C earthquakes we propose that spatiotemporal variations in the occurrence of such events could produce a continuous signal of background uplift over millennial time scales. This would support the hypothesis proposed by Melnick (2016) that accumulation of anelastic deformation occurs down-dip of the interseismically locked megathrust. Maximum coseismic displacements along the coast vary between 309 and 386 mm for the considered earthquakes (Figure 7a). A recurrence time of 88 years of domain-C earthquakes would therefore be needed to account for a background-uplift rate of 0.225 mm/yr during the last 125 kyr (using a median coseismic uplift of 318 mm). Although the occurrence of such major and deep earthquakes has not yet been recorded continuously along the western South American coast, we consider the calculated recurrence time to be reasonable, due to similar recurrence times of 82–123 years for M7.7–M8 earthquakes based on Gutenberg-Richter distributions in northern Chile (Sippl et al., 2019). We hypothesize that major, deep earthquakes are responsible for permanent coastal uplift. However, a caveat for our hypothesis is that the available seismicity catalogs are incomplete, especially for parts of the Peruvian and Ecuadorian margins (e.g., USGS earthquake catalog). Although domain-C earthquakes are characteristic of the entire South American margin (Figure S5 in Supporting Information S1; ISC-GEM earthquake catalog, Di Giacomo et al., 2018), their spatially disparate nature makes further validation of this hypothesis necessary.
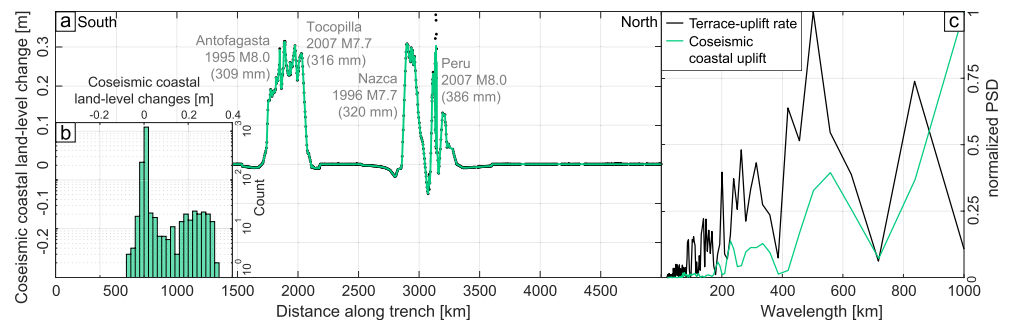
Figure 7. Cumulative vertical displacements of major domain-C earthquakes extracted at the coastline and projected along the trench (a), primarily showing coseismic uplift when plotted in a histogram (b). Maximum coseismic displacement at the coast is stated in parentheses below each earthquake. (c) Wavelength spectrum of coseismic coastal land-level changes demonstrating a significant correlation with the spectrum of terrace-uplift rate.

6. Conclusions

In this study, we tested the impact of various tectonic mechanisms and related parameters with respect to the accumulation of permanent forearc deformation along the western South American coast. Our previously compiled database of ∼2,000 elevation measurements of uplifted marine terraces affords a unique opportunity to analyze long-term coastal deformation since the last interglacial (∼125 kyr) at a continental scale. Spectral analysis of the uplift-rate signal and its correlation with selected tectonic parameters provides new insights into possible contributions of tectonic processes that act on different spatial and temporal scales. The available database also allowed us to test various mechanisms that might explain the continuous background uplift characterizing the coast of western South America. Our main findings are as follows:

1. The uplift-rate signal along the western South American coast is characterized by a constant background signal (median: 0.225 mm/yr), which is perturbed by short-wavelength (∼20 km) to long-wavelength (∼850 km) variations.
2. Similarities between the wavelength spectra of uplift rate and those of several tectonic signals suggest potential correlations: short-wavelength signals in uplift rate are primarily caused by the effects of local crustal faulting (22.5–66.2 km), while intermediate-wavelength to long-wavelength variations in uplift rate correlate with tectonic parameters indicating various extents of locked areas of the megathrust that are likely related to its long-term seismotectonic segmentation. The spectral correlation of terrace-uplift rates with cumulative coseismic displacements suggests accumulation of permanent deformation during individual seismic events, especially for major earthquakes with focal depths near the Moho.
3. With respect to the continuous background signal of uplift revealed in our analysis, we did not find a direct link between interseismic and long-term coastal uplift at continental scale, even when crustal faulting is taken into account. However, coastal uplift resulting from major earthquakes near the Moho (M7–M8, ∼35–55-km depth) might explain the accumulation of anelastic deformation. Although records of such events are sparse, this mechanism is supported by a good spectral correlation of terrace-uplift rates and moderate coseismic uplift that reveals similar recurrence times for the last interglacial period according to current Gutenberg-Richter distributions.
4. Since domain-C earthquakes do not affect coastal regions continuously, we propose that accumulation of permanent deformation arises from multiple, spatially distributed and temporally distinct phases of uplift that add up over millennial time scales.
5. The application of our novel signal-analysis approach provides a useful tool to elucidate the mechanisms driving surface deformation at convergent margins at continental scale, with potential application to tectonic environments elsewhere.

Data Availability Statement

The terrace-elevation database used for the calculation of the uplift-rate signal is published in Freisleben et al. (2020). Topographic calculations and outputs were processed and elaborated in MATLAB® using Topo-Toolbox 2 (Schwanghart & Scherler, 2014).

References

Adam, J., & Reuther, C.-D. (2000). Crustal dynamics and active fault mechanics during subduction erosion. Application of frictional wedge analysis on to the North Chilean Forearc. *Tectonophysics*, *321*(3), 297–325. https://doi.org/10.1016/S0040-1951(00)00074-3

Allmendinger, R. W., & González, G. (2010). Neogene to Quaternary tectonics of the coastal Cordillera, northern Chile. *Tectonophysics*, *495*(1–2), 93–110. https://doi.org/10.1016/j.tecto.2009.04.019

Alvarado, A., Audin, L., Nocquet, J. M., Jaillard, E., Mothes, P., Jarrín, P., et al. (2016). Partitioning of oblique convergence in the Northern Andes subduction zone: Migration history and the present-day boundary of the North Andean Sliver in Ecuador. *Tectonics*, *35*, 1048–1065. https://doi.org/10.1002/2016TC004117

Armijo, R., Lacassin, R., Coudurier-Curveur, A., & Carrizo, D. (2015). Coupled tectonic evolution of Andean orogeny and global climate. *Earth-Science Reviews*, *143*, 1–35. https://doi.org/10.1016/j.earscirev.2015.01.005

Armijo, R., & Thiele, R. (1990). Active faulting in northern Chile: Ramp stacking and lateral decoupling along a subduction plate boundary? *Earth and Planetary Science Letters*, *98*(1), 40–61. https://doi.org/10.1016/0012-821X(90)90087-E

Audin, L., Lacan, P., Tavera, H., & Bondoux, F. (2008). Upper plate deformation and seismic barrier in front of Nazca subduction zone: The Chololo fault system and active tectonics along the Coastal Cordillera, southern Peru. *Tectonophysics*, *459*(1–4), 174–185. https://doi.org/10.1016/j.tecto.2007.11.070

Baize, S., Audin, L., Winter, T., Alvarado, A., Pilatasig Moreno, L., Taipe, M., et al. (2015). Paleoseismology and tectonic geomorphology of the Pallatanga fault (Central Ecuador), a major structure of the South-American crust. *Geomorphology*, *237*, 14–28. https://doi.org/10.1016/j.geomorph.2014.02.030

Bangs, N. L., Morgan, J. K., Tréhu, A. M., Contreras-Reyes, E., Arnulf, A. F., Han, S., et al. (2020). Basal accretion along the South Central Chilean margin and its relationship to great earthquakes. *Journal of Geophysical Research: Solid Earth*, *125*, e2020JB019861. https://doi.org/10.1029/2020JB019861

Bassett, D., & Watts, A. B. (2015). Gravity anomalies, crustal structure, and seismicity at subduction zones: 1. Seafloor roughness and subducting relief. *Geochemistry, Geophysics, Geosystems*, *16*, 1508–1540. https://doi.org/10.1002/2014GC005684

Beck, S., Barrientos, S., Kausel, E., & Reyes, M. (1998). Source characteristics of historic earthquakes along the central Chile subduction zone. *Journal of South American Earth Sciences*, *11*(2), 115–129. https://doi.org/10.1016/S0895-9811(98)00005-4

Cisternas, M., Atwater, B. F., Torrejón, F., Sawai, Y., Machuca, G., Lagos, M., et al. (2005). Predecessors of the giant 1960 Chile earthquake. *Nature*, *437*(7057), 404–407. https://doi.org/10.1038/nature03943

Clift, P. D., & Hartley, A. J. (2007). Slow rates of subduction erosion and coastal underplating along the Andean margin of Chile and Peru. *Geology*, *35*(6), 503–506. https://doi.org/10.1130/G23584A.1

Collot, J.-Y., Sanclemente, E., Nocquet, J.-M., Leprêtre, A., Ribodetti, A., Jarrin, P., et al. (2017). Subducted oceanic relief locks the shallow megathrust in central Ecuador. *Journal of Geophysical Research: Solid Earth*, *122*, 3286–3305. https://doi.org/10.1002/2016JB013849

Comte, D., & Pardo, M. (1991). Reappraisal of great historical earthquakes in the northern Chile and southern Peru seismic gaps. *Natural Hazards*, *4*(1), 23–44. https://doi.org/10.1007/BF00126557

Costa, C., Alvarado, A., Audemard, F., Audin, L., Benavente, C., Bezerra, F. H., et al. (2020). Hazardous faults of South America; compilation and overview. *Journal of South American Earth Sciences*, *104*(1), 102837. https://doi.org/10.1016/j.jsames.2020.102837

Costa, C., Machette, M. N., Dart, R. L., Bastias, H. E., Paredes, J. D., Perucca, L. P., et al. (2000). *Map and database of Quaternary faults and folds in Argentina (Open-File Report)*. US Geological Survey. https://doi.org/10.3133/ofr00108

Cubas, N., Avouac, J.-P., Souloumiac, P., & Leroy, Y. (2013). Megathrust friction determined from mechanical analysis of the forearc in the Maule earthquake area. *Earth and Planetary Science Letters*, *381*, 92–103. https://doi.org/10.1016/j.epsl.2013.07.037

Dahlen, F. A. (1984). Noncohesive critical Coulomb wedges: An exact solution. *Journal of Geophysical Research*, *89*(B12), 10125–10133. https://doi.org/10.1029/JB089iB12p10125

Darwin, C. R. (1846). *Geological observations on South America. Being the third part of the geology of the voyage of the Beagle, under the command of Capt. Fitzroy, R.N. during the years 1832 to 1836*. Smith Elder and Co.

Di Giacomo, D., Engdahl, E. R., & Storchak, D. A. (2018). The ISC-GEM Earthquake Catalogue (1904–2014): Status after the extension project. *Earth System Science Data*, *10*(4), 1877–1899. https://doi.org/10.5194/essd-10-1877-2018

Dumas, B., Hoang, C. T., & Raffy, J. (2006). Record of MIS 5 sea-level highstands based on U/Th dated coral terraces of Haiti. *Quaternary International*, *145–146*, 106–118. https://doi.org/10.1016/j.quaint.2005.07.010

Ferranti, L., Antonioli, F., Anzidei, M., Monaco, C., & Stocchi, P. (2010). The timescale and spatial extent of recent vertical tectonic motions in Italy: Insights from relative sea-level changes studies. *Journal of the Virtual Explorer*, *36*, 30. https://doi.org/10.3809/jvirtex.2010.00255

Ferranti, L., Antonioli, F., Mauz, B., Amorosi, A., Dai Pra, G., Mastronuzzi, G., et al. (2006). Markers of the last interglacial sea-level high stand along the coast of Italy: Tectonic implications. *Quaternary International*, *145–146*(2), 30–54. https://doi.org/10.1016/j.quaint.2005.07.009

Freisleben, R., Jara-Muñoz, J., Melnick, D., Martínez, J. M., & Strecker, M. R. (2020). Marine terraces of the last interglacial period along the Pacific coast of South America (1°N–40°S) [Dataset]. Zenodo. https://doi.org/10.5281/ZENODO.4309748

Freisleben, R., Jara-Muñoz, J., Melnick, D., Martínez, J. M., & Strecker, M. R. (2021). Marine terraces of the last interglacial period along the Pacific coast of South America (1°N–40°S). *Earth System Science Data*, *13*(6), 2487–2513. https://doi.org/10.5194/essd-13-2487-2021

Gardner, T. W., Fisher, D. M., Morell, K. D., & Cupper, M. L. (2013). Upper-plate deformation in response to flat slab subduction inboard of the aseismic Cocos Ridge, Osa Peninsula, Costa Rica. *Lithosphere*, *5*(3), 247–264. https://doi.org/10.1130/L251.1

GEBCO Bathymetric Compilation Group. (2020). *The GEBCO_2020 grid—A continuous terrain model of the global oceans and land: British Oceanographic data Centre*. National Oceanography Centre.

Glodny, J., Lohrmann, J., Echtler, H., Gräfe, K., Seifert, W., Collao, S., & Figueroa, O. (2005). Internal dynamics of a paleoaccretionary wedge: Insights from combined isotope tectonochronology and sandbox modelling of the South-central Chilean forearc. *Earth and Planetary Science Letters*, *231*(1–2), 23–39. https://doi.org/10.1016/j.epsl.2004.12.014

González-Alfaro, J., Vargas, G., Ortlieb, L., González, G., Ruiz, S., Báez, J. C., et al. (2018). Abrupt increase in the coastal uplift and earthquake rate since ∼40 ka at the northern Chile seismic gap in the Central Andes. *Earth and Planetary Science Letters*, *502*, 32–45. https://doi.org/10.1016/j.epsl.2018.08.043

Graham, S. E., Loveless, J. P., & Meade, B. J. (2018). Global Plate motions and earthquake cycle effects. *Geochemistry, Geophysics, Geosystems*, *19*, 2032–2048. https://doi.org/10.1029/2017GC007391

Gusman, A. R., Murotani, S., Satake, K., Heidarzadeh, M., Gunawan, E., Watada, S., & Schurr, B. (2015). Fault slip distribution of the 2014 Iquique, Chile, earthquake estimated from ocean-wide tsunami waveforms and GPS data. *Geophysical Research Letters*, *42*, 1053–1060. https://doi.org/10.1002/2014GL062604

Gutscher, M.-A., Malavieille, J., Lallemand, S., & Collot, J.-Y. (1999). Tectonic segmentation of the North Andean margin: Impact of the Carnegie Ridge collision. *Earth and Planetary Science Letters*, *168*(3–4), 255–270. https://doi.org/10.1016/S0012-821X(99)00060-6

Hampel, A. (2002). The migration history of the Nazca Ridge along the Peruvian active margin: A re-evaluation. *Earth and Planetary Science Letters*, *203*(2), 665–679. https://doi.org/10.1016/S0012-821X(02)00859-2

Hayes, G. P. (2017). The finite, kinematic rupture properties of great-sized earthquakes since 1990. *Earth and Planetary Science Letters*, *468*(3), 94–100. https://doi.org/10.1016/j.epsl.2017.04.003

Hayes, G. P., Moore, G. L., Portner, D. E., Hearne, M., Flamme, H., Furtney, M., & Smoczyk, G. M. (2018). Slab2, a comprehensive subduction zone geometry model. *Science*, *362*(6410), 58–61. https://doi.org/10.1126/science.aat4723

Hearty, P. J., Hollin, J. T., Neumann, A. C., O'Leary, M. J., & McCulloch, M. (2007). Global sea-level fluctuations during the last interglaciation (MIS 5e). *Quaternary Science Reviews*, *26*(17–18), 2090–2112. https://doi.org/10.1016/j.quascirev.2007.06.019

Hsu, J. T. (1992). Quaternary uplift of the Peruvian coast related to the subduction of the Nazca Ridge: 13.5 to 15.6 degrees south latitude. *Quaternary International*, *15–16*, 87–97. https://doi.org/10.1016/1040-6182(92)90038-4

Jaillard, E., Hérail, G., Monfret, T., Díaz-Martínez, E., Baby, P., Lavenu, A., & Dumont, J. F. (2000). Tectonic evolution of the Andes of Ecuador, Peru, Bolivia, and northernmost Chile. In U. G. Cordani, E. J. Milani, F. A. Thomaz, & D. A. Campos (Eds.), *Tectonic evolution of South America* (31st ed., pp. 481–559). Sociedad Brasileira de Geologia.

Jara-Muñoz, J., Melnick, D., Brill, D., & Strecker, M. R. (2015). Segmentation of the 2010 Maule Chile earthquake rupture from a joint analysis of uplifted marine terraces and seismic-cycle deformation patterns. *Quaternary Science Reviews*, *113*, 171–192. https://doi.org/10.1016/j.quascirev.2015.01.005

Jara-Muñoz, J., Melnick, D., Zambrano, P., Rietbrock, A., González, J., Argandoña, B., & Strecker, M. R. (2017). Quantifying offshore fore-arc deformation and splay-fault slip using drowned Pleistocene shorelines, Arauco Bay, Chile. *Journal of Geophysical Research: Solid Earth*, *122*, 4529–4558. https://doi.org/10.1002/2016JB013339

Jolivet, R., Simons, M., Duputel, Z., Olive, J. A., Bhat, H. S., & Bletery, Q. (2020). Interseismic loading of subduction megathrust drives long-term uplift in Northern Chile. *Geophysical Research Letters*, *47*, e2019GL085377. https://doi.org/10.1029/2019GL085377

Jordan, T. E., Isacks, B. L., Allmendinger, R. W., Brewer, J. A. O. N., Ramos, V. A., & Ando, C. J. (1983). Andean tectonics related to geometry of subducted Nazca plate. *Geological Society of America Bulletin*, *94*(3), 341–361. https://doi.org/10.1130/0016-7606(1983)94<341:ATRTGO>2.0.CO;2

Kelsey, H. M., Ticknor, R. L., Bockheim, J. G., & Mitchell, E. (1996). Quaternary upper plate deformation in coastal Oregon. *Geological Society of America Bulletin*, *108*(7), 843–860. https://doi.org/10.1130/0016-7606(1996)108<0843:QUPDIC>2.3.CO;2

Kendrick, E., Bevis, M., Smalley, R., Brooks, B., Vargas, R. B., Laurı́a, E., & Fortes, L. P. S. (2003). The Nazca-South America Euler vector and its rate of change. *Journal of South American Earth Sciences*, *16*(2), 125–131. https://doi.org/10.1016/S0895-9811(03)00028-2

Lajoie, K. R. (1986). Coastal tectonics. In R. E. Wallace (Ed.), *Studies in geophysics. Active tectonics* (pp. 95–124). National Academics Press.

Lay, T., Kanamori, H., Ammon, C. J., Koper, K. D., Hutko, A. R., Ye, L., et al. (2012). Depth-varying rupture properties of subduction zone megathrust faults. *Journal of Geophysical Research*, *117*, B04311. https://doi.org/10.1029/2011JB009133

Lehner, F. K. (1986). Comments on "Noncohesive critical Coulomb wedges: An exact solution" by F. A. Dahlen. *Journal of Geophysical Research*, *91*(B1), 793–796. https://doi.org/10.1029/JB091iB01p00793

Lomnitz, C. (2004). Major Earthquakes of Chile: A historical survey, 1535–1960. *Seismological Research Letters*, *75*(3), 368–378. https://doi.org/10.1785/gssrl.75.3.368

Madella, A., & Ehlers, T. A. (2021). Contribution of background seismicity to forearc uplift. *Nature Geoscience*, *14*(8), 620–625. https://doi.org/10.1038/s41561-021-00779-0

Malatesta, L. C., Bruhat, L., Finnegan, N. J., & Olive, J. A. L. (2021). Co-location of the downdip end of seismic coupling and the continental shelf break. *Journal of Geophysical Research: Solid Earth*, *126*, e2020JB019589. https://doi.org/10.1029/2020JB019589

Maldonado, V., Contreras, M., & Melnick, D. (2021). A comprehensive database of active and potentially-active continental faults in Chile at 1:25,000 scale. *Scientific Data*, *8*(1), 20. https://doi.org/10.1038/s41597-021-00802-4

Mann, P., Taylor, F. W., Lagoe, M. B., Quarles, A., & Burr, G. (1998). Accelerating late Quaternary uplift of the New Georgia Island Group (Solomon island arc) in response to subduction of the recently active Woodlark spreading center and Coleman seamount. *Tectonophysics*, *295*(3–4), 259–306. https://doi.org/10.1016/S0040-1951(98)00129-2

Margirier, A., Strecker, M. R., Reiners, P. W., Thomson, S. N., Casado, I., George, S. W. M., & Alvarado, A. (2023). Late miocene exhumation of the western Cordillera, Ecuador, driven by increased coupling between the subducting Carnegie Ridge and the South American continent. *Tectonics*, *42*, e2022TC007344. https://doi.org/10.1029/2022TC007344

Martinod, J., Regard, V., Letourmy, Y., Henry, H., Hassani, R., Baratchart, S., & Carretier, S. (2016). How do subduction processes contribute to forearc Andean uplift? Insights from numerical models. *Journal of Geodynamics*, *96*, 6–18. https://doi.org/10.1016/j.jog.2015.04.001

Matsu'ura, T. (2015). Late Quaternary uplift rate inferred from marine terraces, Muroto Peninsula, southwest Japan: Forearc deformation in an oblique subduction zone. *Geomorphology*, *234*(B5), 133–150. https://doi.org/10.1016/j.geomorph.2015.01.012

Matsu'ura, T., Komatsubara, J., & Wu, C. (2019). Accurate determination of the Pleistocene uplift rate of the NE Japan forearc from the buried MIS 5e marine terrace shoreline angle. *Quaternary Science Reviews*, *212*(3–4), 45–68. https://doi.org/10.1016/j.quascirev.2019.03.007

McKenzie, K. A., Kelsey, H. M., Kirby, E., Rittenour, T. M., & Furlong, K. P. (2022). Differential coastal uplift quantified by luminescence dating of marine terraces, central Cascadia forearc, Oregon. *Quaternary Science Reviews*, *298*(4), 107853. https://doi.org/10.1016/j.quascirev.2022.107853

Melnick, D. (2016). Rise of the central Andean coast by earthquakes straddling the Moho. *Nature Geoscience*, *9*(5), 401–407. https://doi.org/10.1038/ngeo2683

Melnick, D., Bookhagen, B., Echtler, H. P., & Strecker, M. R. (2006). Coastal deformation and great subduction earthquakes, Isla Santa Maria, Chile (37°S). *Geological Society of America Bulletin*, *118*(11–12), 1463–1480. https://doi.org/10.1130/B25865.1

Melnick, D., Bookhagen, B., Strecker, M. R., & Echtler, H. P. (2009). Segmentation of megathrust rupture zones from fore-arc deformation patterns over hundreds to millions of years, Arauco peninsula, Chile. *Journal of Geophysical Research*, *114*, B01407. https://doi.org/10.1029/2008JB005788

Melnick, D., & Echtler, H. P. (2006). Inversion of forearc basins in south-central Chile caused by rapid glacial age trench fill. *Geology*, *34*(9), 709–712. https://doi.org/10.1130/G22440.1

Melnick, D., Hillemann, C., Jara-Muñoz, J., Garrett, E., Cortés-Aranda, J., Molina, D., et al. (2019). Hidden Holocene slip along the coastal El Yolki Fault in Central Chile and its possible link with megathrust earthquakes. *Journal of Geophysical Research: Solid Earth*, *124*, 7280–7302. https://doi.org/10.1029/2018JB017188

Menant, A., Angiboust, S., Gerya, T., Lacassin, R., Simoes, M., & Grandin, R. (2020). Transient stripping of subducting slabs controls periodic forearc uplift. *Nature Communications*, *11*(1), 1823. https://doi.org/10.1038/s41467-020-15580-7

Métois, M., Vigny, C., & Socquet, A. (2016). Interseismic coupling, megathrust earthquakes and seismic swarms along the Chilean subduction zone (38°–18°S). *Pure and Applied Geophysics*, *173*(5), 1431–1449. https://doi.org/10.1007/s00024-016-1280-5

Molina, D., Tassara, A., Abarca, R., Melnick, D., & Madella, A. (2021). Frictional segmentation of the Chilean megathrust from a multivariate analysis of geophysical, geological, and geodetic data. *Journal of Geophysical Research: Solid Earth*, *126*, e2020JB020647. https://doi.org/10.1029/2020JB020647

Muhs, D. R., Simmons, K. R., Kennedy, G. L., & Rockwell, T. K. (2002). The last interglacial period on the Pacific Coast of North America: Timing and paleoclimate. *Geological Society of America Bulletin*, *114*(5), 569–592. https://doi.org/10.1130/0016-7606(2002)114<0569:TLIPOT>2.0.CO;2

Muhs, D. R., Simmons, K. R., Schumann, R. R., Groves, L. T., DeVogel, S. B., Minor, S. A., & Laurel, D. (2014). Coastal tectonics on the eastern margin of the Pacific Rim: Late Quaternary sea-level history and uplift rates, channel Islands National Park, California, USA. *Quaternary Science Reviews*, *105*(7), 209–238. https://doi.org/10.1016/j.quascirev.2014.09.017

Naranjo, J. A. (1987). Interpretacion de la actividad cenozoica superior a lo largo de la zona de Falla Atacama, Norte de Chile. *Revista Geologica de Chile*(31), 43–55.

Ocola, L. (2008). Southern Perú coseismic subsidence: 23 June 2001 8.4-Mw earthquake. *Advances in Geosciences*, *14*, 79–83. https://doi.org/10.5194/adgeo-14-79-2008

Okada, Y. (1992). Internal deformation due to shear and tensile faults in a half-space. *Bulletin of the Seismological Society of America*, *82*(2), 1018–1040. https://doi.org/10.1785/BSSA0820021018

Pedoja, K., Dumont, J. F., Lamothe, M., Ortlieb, L., Collot, J.-Y., Ghaleb, B., et al. (2006). Plio-quaternary uplift of the Manta peninsula and La Plata island and the subduction of the Carnegie Ridge, central coast of Ecuador. *Journal of South American Earth Sciences*, *22*(1–2), 1–21. https://doi.org/10.1016/j.jsames.2006.08.003

Pedoja, K., Husson, L., Johnson, M. E., Melnick, D., Witt, C., Pochat, S., et al. (2014). Coastal staircase sequences reflecting sea-level oscillations and tectonic uplift during the Quaternary and Neogene. *Earth-Science Reviews*, *132*, 13–38. https://doi.org/10.1016/j.earscirev.2014.01.007

Pedoja, K., Husson, L., Regard, V., Cobbold, P. R., Ostanciaux, E., Johnson, M. E., et al. (2011). Relative sea-level fall since the last interglacial stage: Are coasts uplifting worldwide? *Earth-Science Reviews*, *108*(1–2), 1–15. https://doi.org/10.1016/j.earscirev.2011.05.002

Philibosian, B., & Meltzner, A. J. (2020). Segmentation and supercycles: A catalog of earthquake rupture patterns from the Sumatran Sunda megathrust and other well-studied faults worldwide. *Quaternary Science Reviews*, *241*(27), 106390. https://doi.org/10.1016/j.quascirev.2020.106390

Regard, V., Saillard, M., Martinod, J., Audin, L., Carretier, S., Pedoja, K., et al. (2010). Renewed uplift of the central Andes forearc revealed by coastal evolution during the Quaternary. *Earth and Planetary Science Letters*, *297*(1–2), 199–210. https://doi.org/10.1016/j.epsl.2010.06.020

Remy, D., Perfettini, H., Cotte, N., Avouac, J. P., Chlieh, M., Bondoux, F., et al. (2016). Postseismic relocking of the subduction megathrust following the 2007 Pisco, Peru, earthquake. *Journal of Geophysical Research: Solid Earth*, *121*, 3978–3995. https://doi.org/10.1002/2015JB012417

Rohling, E. J., Grant, K., Bolshaw, M., Roberts, A. P., Siddall, M., Hemleben, C., & Kucera, M. (2009). Antarctic temperature and global sea level closely coupled over the past five glacial cycles. *Nature Geoscience*, *2*(7), 500–504. https://doi.org/10.1038/ngeo557

Rousset, B., Lasserre, C., Cubas, N., Graham, S., Radiguet, M., DeMets, C., et al. (2016). Lateral variations of interplate coupling along the Mexican subduction interface: Relationships with long-term morphology and fault zone mechanical properties. *Pure and Applied Geophysics*, *173*(10–11), 3467–3486. https://doi.org/10.1007/s00024-015-1215-6

Saillard, M., Audin, L., Rousset, B., Avouac, J.-P., Chlieh, M., Hall, S. R., et al. (2017). From the seismic cycle to long-term deformation: Linking seismic coupling and quaternary coastal geomorphology along the Andean megathrust. *Tectonics*, *36*, 241–256. https://doi.org/10.1002/2016TC004156

Saillard, M., Hall, S. R., Audin, L., Farber, D. L., Regard, V., & Hérail, G. (2011). Andean coastal uplift and active tectonics in southern Peru: ^{10}Be surface exposure dating of differentially uplifted marine terrace sequences (San Juan de Marcona, ~15.4°S). *Geomorphology*, *128*(3–4), 178–190. https://doi.org/10.1016/j.geomorph.2011.01.004

Sak, P. B., Fisher, D. M., & Gardner, T. W. (2004). Effects of subducting seafloor roughness on upper plate vertical tectonism: Osa Peninsula, Costa Rica. *Tectonics*, *23*, TC1017. https://doi.org/10.1029/2002TC001474

Sandwell, D. T., Müller, R. D., Smith, W. H. F., Garcia, E., & Francis, R. (2014). New global marine gravity model from CryoSat-2 and Jason-1 reveals buried tectonic structure. *Science*, *346*(6205), 65–67. https://doi.org/10.1126/science.1258213

Santibáñez, I., Cembrano, J., García-Pérez, T., Costa, C., Yáñez, G., Marquardt, C., et al. (2019). Crustal faults in the Chilean Andes: Geological constraints and seismic potential. *Andean Geology*, *46*(1), 32. https://doi.org/10.5027/andgeoV46n1-3067

Schurr, B., Asch, G., Hainzl, S., Bedford, J., Hoechner, A., Palo, M., et al. (2014). Gradual unlocking of plate boundary controlled initiation of the 2014 Iquique earthquake. *Nature*, *512*(7514), 299–302. https://doi.org/10.1038/nature13681

Schwanghart, W., & Scherler, D. (2014). Short communication: TopoToolbox 2—MATLAB-based software for topographic analysis and modeling in Earth surface sciences. *Earth Surface Dynamics*, *2*(1), 1–7. https://doi.org/10.5194/esurf-2-1-2014

Shackleton, N. J., Sánchez-Goñi, M. F., Pailler, D., & Lancelot, Y. (2003). Marine isotope substage 5e and the Eemian interglacial. *Global and Planetary Change*, *36*(3), 151–155. https://doi.org/10.1016/S0921-8181(02)00181-9

Siddall, M., Chappell, J., & Potter, E.-K. (2006). Eustatic sea level during past interglacials. In F. Sirocko, T. Litt, M. Claussen, & M.-F. Sanchez-Goni (Eds.), *The climate of past interglacials* (pp. 75–92). Elsevier. https://doi.org/10.1016/S1571-0866(07)80032-7

Simms, A. R., Rood, D. H., & Rockwell, T. K. (2020). Correcting MIS5e and 5a sea-level estimates for tectonic uplift, an example from southern California. *Quaternary Science Reviews*, *248*, 106571. https://doi.org/10.1016/j.quascirev.2020.106571

Singh, S. C., Hananto, N., Mukti, M., Robinson, D. P., Das, S., Chauhan, A., et al. (2011). Aseismic zone and earthquake segmentation associated with a deep subducted seamount in Sumatra. *Nature Geoscience*, *4*(5), 308–311. https://doi.org/10.1038/ngeo1119

Sippl, C., Schurr, B., John, T., & Hainzl, S. (2019). Filling the gap in a double seismic zone: Intraslab seismicity in Northern Chile. *Lithos*, *346–347*, 105155. https://doi.org/10.1016/j.lithos.2019.105155

Stirling, C. H., Esat, T. M., Lambeck, K., & McCulloch, M. T. (1998). Timing and duration of the last interglacial: Evidence for a restricted interval of widespread coral reef growth. *Earth and Planetary Science Letters*, *160*(3–4), 745–762. https://doi.org/10.1016/S0012-821X(98)00125-3

Styron, R., & Pagani, M. (2020). The GEM global active faults database. *Earthquake Spectra*, *36*(Suppl. 1), 160–180. https://doi.org/10.1177/8755293020944182

Suárez, G., Molnar, P., & Burchfiel, B. C. (1983). Seismicity, fault plane solutions, depth of faulting, and active tectonics of the Andes of Peru, Ecuador, and southern Colombia. *Journal of Geophysical Research*, *88*(B12), 10403–10428. https://doi.org/10.1029/JB088iB12p10403

Tam, E., & Yokoyama, Y. (2021). A review of MIS 5e sea-level proxies around Japan. *Earth System Science Data*, *13*(4), 1477–1497. https://doi.org/10.5194/essd-13-1477-2021

Udias, A., Madariaga, R., Buforn, E., Munoz, D., & Ros, M. (2012). The large Chilean historical earthquakes of 1647, 1657, 1730, and 1751 from contemporary documents. *Bulletin of the Seismological Society of America*, *102*(4), 1639–1653. https://doi.org/10.1785/0120110289

Veloza, G., Styron, R., Taylor, M., & Mora, A. (2012). Open-source archive of active faults for northwest South America. *Geological Society of America Today*, *22*(10), 4–10. https://doi.org/10.1130/GSAT-G156A.1

Villegas-Lanza, J. C., Chlieh, M., Cavalié, O., Tavera, H., Baby, P., Chire-Chira, J., & Nocquet, J.-M. (2016). Active tectonics of Peru: Heterogeneous interseismic coupling along the Nazca megathrust, rigid motion of the Peruvian Sliver, and Subandean shortening accommodation. *Journal of Geophysical Research: Solid Earth*, *121*, 7371–7394. https://doi.org/10.1002/2016JB013080

Wang, K., & Bilek, S. L. (2011). Do subducting seamounts generate or stop large earthquakes? *Geology*, *39*(9), 819–822. https://doi.org/10.1130/G31856.1

Wang, K., & Bilek, S. L. (2014). Invited review paper: Fault creep caused by subduction of rough seafloor relief. *Tectonophysics*, *610*, 1–24. https://doi.org/10.1016/j.tecto.2013.11.024

Wesson, R. L., Melnick, D., Cisternas, M., Moreno, M., & Ely, L. L. (2015). Vertical deformation through a complete seismic cycle at Isla Santa María, Chile. *Nature Geoscience*, *8*(7), 547–551. https://doi.org/10.1038/ngeo2468